(Received 16 August 2025, Accepted 14 November 2025, Scheduled 2 January 2026)

Design and Implementation of Metamaterial Inspired Reconfigurable Multiband Antenna for 5G/Sub 6 GHz NR and Wireless Applications

Hareetaa Mallani[1,*], Archana Agrawal[1], and Ritesh K. Saraswat[2]

[1]*Sangam University, Bhilwara (Rajasthan), India*
[2]*M.L.V. Govt. Textile & Engineering College, Bhilwara (Rajasthan), India*

ABSTRACT: In this article, the authors propose the design and implementation of a frequency reconfigurable metamaterial-inspired octagon-shaped antenna for multiple wireless standards. The multiband functionality is achieved by incorporating a slotted self-similar octagonal radiating part with two SRR cells. The antenna design incorporates PIN diode switching elements on the slotted radiating patch, along with metamaterial-based SRR cell loading and a modified trapezoid-shaped partial ground plane, enabling its use across multiple wireless standards. The proposed design is resonating across five microwave frequency bands, including S-band WiMAX (3.5 GHz — IEEE 802.16e), 5G NR bands (n48: 3.55–3.70 GHz, n46: 5.15–5.925 GHz, n47: 5.855–5.925 GHz, n77: 3.3–4.2 GHz, n78: 3.3–3.8 GHz, n79: 4.4–5.0 GHz), C-band WLAN (5.0/5.8 GHz — IEEE 802.11a/ac), X-band (satellite communication, radar, terrestrial broadband, space communication), lower Ku-band for radar communication (13.43–14.55 GHz), upper Ku-band for molecular rotational spectroscopy (17.25–18.32 GHz), and lower K-band for astronomical observation services (18.81–19.96 GHz). The multiband antenna is then fabricated and tested, with measured and simulated results for return loss, gain, radiation efficiency, E-plane, and H-plane showing good agreement. The antenna's penta-band operation, compact size, stable radiation characteristics, and good impedance across the entire resonating band make it well-suited for various wireless applications.

1. INTRODUCTION

Recently, advancements in multiband and miniaturization technologies for antenna design have accelerated significantly. Implementing a multiband antenna approach in smartphones enables operation across different wireless communication standards. Various techniques are available to achieve multiband functionality and miniaturization within a single antenna design, including feeding methods [1–3], slotted radiating/ground sections [4–9], metamaterial loading [10–14], and the fractalization approach [15]. The slotted patch/ground plane formation helps achieve antenna miniaturization while adding resonant bands for various wireless applications by inducing electric current perturbation [16–18]. Additionally, the metamaterial loading method has gained substantial attention in multiband smart antenna design, as it increases the number of resonant bands. The growing interest in metamaterials is attributed to their unique properties of negative permeability and permittivity. Numerous metamaterial-inspired multiband antennas have been published and reported in the literature [19–22]. For instance, Sharma et al. [19] developed a metamaterial-loaded triple-band antenna for WLAN and WiMAX. Similarly, in [20–22], metamaterial split ring resonator (SRR)-based multiband antennas were proposed for multiple wireless applications. Ali et al. [23] designed a quad-band antenna, achieving size miniaturization and bandwidth enhancement by incorporating slot etching, fractalization, and metamaterial loading techniques.

The hybrid integration of metamaterials and fractal sections in antenna design proves effective in enhancing impedance matching, gain, radiation efficiency, the number of operating bands, and bandwidth [24–28]. In [29], researchers demonstrated an antenna design that achieved gain improvement and size reduction through the use of SRR. A compact metamaterial-inspired open split-ring resonator (OSRR) antenna, offering a 38.83% size reduction, is proposed for multiband operation, covering WLAN, WiMAX, and X-band applications [30]. Additionally, a metamaterial-loaded multiband antenna with frequency band reconfigurability using a switching element (RF diode) was introduced in [31, 32]. Specifically, in [31], a frequency-reconfigurable, metamaterial-loaded triple-band antenna is developed for WLAN and WiMAX standards. In [32], a vertex-fed antenna with six resonating bands is introduced, showcasing frequency-reconfigurability features designed for various wireless standards. Furthermore, multiband antennas operating over UWB as well as various wireless standards employ a defected ground structure (DGS) along with metamaterial loading were designed for wireless applications [33, 34, 62–66].

Despite the considerable progress in multiband and miniaturized antenna technologies, many existing designs face limitations such as restricted operating bands, insufficient frequency reconfigurability, or trade-offs in size reduction,

* Corresponding author: Hareetaa Mallani (hareetaa@mlvti.ac.in).

TABLE 1. Active radiating section miniaturization calculation for proposed design.

Parameters	Active Patch Area (in mm^2)	Operating Mode
Conventional Antenna	309.02	UWB (3.1–10.6 GHz)
Proposed Antenna (Configuration C)	156.78	WLAN/WiMAX/X/Ku/K
% Miniaturization achieved (w.r.t. conventional antenna)	49.26	Multiple Band

bandwidth, and radiation efficiency. To bridge these gaps, the proposed frequency reconfigurable slotted self-similar patch antenna integrates slotted geometry with metamaterial loading, enabling simultaneous multiband operation, compactness, and enhanced performance. By incorporating two metamaterial cells along with a self-similar slotted structure, the design successfully achieves penta-band characteristics, offering wide coverage across WiMAX, 5G NR bands, WLAN, X-band Earth exploration-satellite services, Amateur satellite bands, Lower and Upper Ku bands, and the Lower K band. This hybrid approach effectively addresses the challenges of conventional multiband designs by combining miniaturization, improved impedance matching, and frequency agility, thereby providing a versatile solution for next-generation wireless communication systems. The proposed structure demonstrated operating bands of 3.21–6.15 GHz (62.82%), 6.97–12.76 GHz (58.69%), 13.43–14.55 GHz (8.01%), 17.25–18.32 GHz (6.02%), and 18.81–19.96 GHz (5.93%) in simulation mode. Under measurement mode, it yielded operating bands of 3.20–5.98 GHz (60.57%), 7.10–12.78 GHz (57.14%), 13.51–14.52 GHz (7.21%), 17.34–18.32 GHz (5.49%), and 18.86–19.96 GHz (5.67%), covering wireless standards such as S-band WiMAX (3.5 GHz), 5G NR bands (n48, n46, n47, n77, n78, n79), C-band WLAN (5.0/5.8 GHz), X-band (8–12 GHz), Lower Ku-band (13.98 GHz radar communication), Upper Ku-band (17.76 GHz molecular rotational spectroscopy), and Lower K-band (19.35 GHz astronomical observations). The frequency reconfigurability is achieved through the use of PIN diodes, which are placed between the slotted hexagonal radiating segments and the edges of the octagonal patch area.

The paper is structured as follows. First, the design evolution of the metamaterial-inspired slotted multiband antenna for wireless applications is presented. It is followed by a detailed design analysis of the proposed octagon-shaped slotted radiating geometry, along with the metamaterial SRR and its impact on antenna performance. Afterward, the frequency band reconfigurability features of the design concerning various wireless standards are implemented. Finally, the fabrication and testing results are discussed and compared with the simulated outcomes.

1.1. Novelty of Proposed Design

The novelty of the proposed design is identified as: (i) The miniaturization of the proposed design is achieved by about 49.26% regarding active patch area (mentioned in Table 1); (ii) Designed/analysed miniaturized multiband antenna is loaded with metamaterial SRR cells to cover the penta band characteristics for wireless applications; (iii) Frequency reconfigurability for various wireless communication applications is achieved by integrating PIN diodes into the design, as outlined in Table 3, which summarizes the different diode states and the corresponding wireless applications; and (iv) Various antenna parameters (gain/radiation efficiency/resonant bands/patterns/size/current distribution) are discussed and compared with related literatures (published multiband antenna) in tabulation form. These parameters are compared with previously published antenna designs in tabular form (Table 2). Finally, the outcomes of the proposed work are concluded.

2. EVOLUTION OF PROPOSED MULTIBAND ANTENNA

This section outlines the evolution stages of the proposed penta-band antenna. The stages, along with the corresponding simulated reflection coefficient (S_{11}), are illustrated in Figures 1 and 2, respectively. The antenna is compact, measuring $29.5 \times 22 \times 1.6\,mm^3$, and is fabricated on a low-cost FR4 substrate with a relative dielectric constant of 4.4 and a loss tangent of 0.02. The use of an octagon-shaped patch radiator in microstrip antenna design offers several advantages over conventional geometries. The octagonal shape naturally supports multiband operation, as its multiple edges and corners introduce additional resonant paths that enhance frequency diversity. This geometry also contributes to antenna miniaturization, allowing lower resonant frequencies to be achieved within a relatively compact footprint, making it suitable for modern wireless and portable devices. Moreover, the symmetrical structure of the octagon improves the current distribution, which enhances impedance bandwidth and provides more stable radiation characteristics with reduced cross-polarization. The geometry further offers flexibility for incorporating slots and metamaterial loading, enabling improvements in gain, bandwidth, and frequency reconfigurability. With appropriate feeding arrangements or perturbations, the octagonal patch can also achieve polarization diversity, supporting both linear and circular polarization, which is highly beneficial for satellite, radar, and mobile communication systems. Additionally, the multiple vertices of the octagon provide natural points for the integration of switching elements, such as PIN diodes or varactors, making it well-suited for reconfigurable antenna designs. Overall, the octagonal patch radiator combines com-

TABLE 2. Comparison of proposed slotted metamaterial inspired multiband antenna with existing work.

Ref.	Year	Dimensions (mm^3)	Operating Bandwidth (%)	Antenna Peak Gain (dBi)	Antenna Radiation Efficiency (%)	Resonant Bands/ Modes	Wireless Applications/ Standards (GHz)	Frequency Reconfiguration Approach	Metamaterial Implementation
[11]	2013	52.6 × 30 × 1	47.27/38.88	– 0.56/– 0.62	89.2/98.1	2	GPS/WLAN	No	Yes
[7]	2014	40 × 40 × 1.6	34.48/18.28/19.96	3.97/4.04/3.25	–	3	WLAN/WiMAX	No	No
[5]	2015	56 × 44 × 0.8	5.56/5.86/ 19.34/13.69	1.3/2.3/ 3.5/4.4	76.8/80.1/ 96.6/85.5	4	GPS/WLAN/ WiMAX	No	No
[6]	2015	40 × 40 × 0.4	12.2/15.4	2.1/3.2	71.2/84.1	2	WLAN/UWB	Yes	No
[31]	2015	27 × 25 × 1.6	18.6/4.3/40.3	0.7/2.1/2.8	–	3	WLAN/WiMAX	Yes	Yes
[12]	2016	48 × 48 × 1.6	20.73/15.02/31.96	1.64/2.07/4.06	66.2/77.15/87.6	3	GPS/WLAN	No	Yes
[13]	2017	19.18 × 22.64 × 1.6	2.4/3.2/12.1	1.36/1.57/1.83	–	3	UMTS/WiMAX/ WLAN	No	Yes
[14]	2018	32 × 38 × 1.6	8/6/5/69.3	3.8 (Avg. Gain)	89% (Avg. Rad. Eff.)	4	WLAN/WiMAX/ ITU/X band	No	Yes
[9]	2018	40 × 40 × 1.5748	15.1/3.45/12.59/ 3.33/3.25/ 5.4/16.58	3.48/3.02/4.49/ 4.25/3.59/ 3.81/5	–	7	WLAN/WiMAX/ PAN/OFDM	No	No
[23]	2018	30 × 24.8 × 1.6	3.5/5.01/ 13.2/5.77	1.35/1/ 1.07/1.75	–	4	WiMAX/ X band	No	Yes
[37]	2018	24 × 24 × 1.28	3.94	–	–	1	WiMAX/ISM	Yes	No
[33]	2019	44 × 39 × 1.6	5.11/7.33/11.70/ 6.38/12.03/5.62	2.72/3.81/2.12/ 2.78/3.68/4.10	41.2/84.7/52.8/ 69.7/78.8/76.9	6	WLAN/WiMAX/C/ X/Ku band	No	No
[32]	2019	44 × 39 × 1.6	5.11/7.33/11.70/ 6.38/12.03/5.62	2.72/3.81/2.12/ 2.78/3.68/4.10	41.2/84.7/52.8/ 69.7/78.8/76.9	6	WLAN/WiMAX/C/ X/Ku band	Yes	No
[36]	2019	30 × 44 × 1.6	11.49/24.48/25.51	1.78/2.12/2.48	75.62/74.45/76.32	3	WLAN/WiMAX	Yes	Yes
[22]	2019	35 × 34 × 1.6	11.81/4.27/4.29/ 6.62/3.27/ 4.22/8.13	1.94/2.2/1.66/ 3.87/3.65/ 4.06/4.14	41.5/48.6/58.1/ 60.1/84.4/ 78.7/82.1	7	WLAN/WiMAX/C/ X/Ku band	No	Yes
[52]	2020	30 × 44 × 1.6	8.80/38.78/ 15.54/35.45	2.63/2.58/ 2.82/2.99	33.5/38.8/ 84.4/72.8	4	WLAN/WiMAX/ WAVE/C/X band	No	Yes
[53]	2021	36 × 32 × 1.6	84/85.32/35.45/ 10.79/15.82	–	–	5	LTE 2300/LTE 2500/ Bluetooth/WLAN/ WiMAX/ITU band	No	No
[54]	2021	50 × 50 × 0.8	16.17/17.85/8.30	5.42/6.52/7.67	–	3	Wi-Fi/WLAN/X-band	No	No
[55]	2022	150 × 75 × 0.8	46.71	5.01	50–63	1	5G NR bands N77/N78/N79	No	No
[56]	2022	150 × 75 × 7.8	60.87	–	38–83	1	5G NR n77/n78/n79 and WLAN	No	No
[57]	2023	58.6 × 58.6 × 0.8	14.08	4.8	76	1	5G NR n77	No	No
[58]	2024	35 × 30 × 1.6	40.8/22.3	3.87/3.93	80.12/82.34	2	Wi-Fi, 5G NR	No	Yes
[59]	2024	31.8 × 27. × 1.6	43/25/15	1.5/4.1/6.5	Less than 75	3	5G NR sub-band, X band, and Ku band	No	Yes
[60]	2024	37 × 22 × 1.6	24.77/14.03/36.04/ 46.21/14.35	2.36/2.72/3.41/ 3.18/4.38	63.56/71.07/48.42/ 69.82/72.87/86.23	5	WLAN, WiMAX, X-band, 5G NR bands, Lower Ku band	No	Yes
Proposed antenna		29.5 × 22 × 1.6	62.82/58.69/8.01/ 6.02/5.93	2.24/3.32/3.72/ 3.21/4.38	62.07/74.18/80.78/ 81.12/84.98	5	WiMAX, WLAN, 5G NR, Lower and upper Ku band, Lower K band	Yes	Yes

TABLE 3. Frequency reconfiguration: PIN diode biasing states demonstrating the associated frequency bands and their applications.

PIN diode biasing states	Frequency bands (in GHz)		10-dB bandwidth (%)		Achieved wireless standards
	Sim.	Meas.	Sim.	Meas.	
D_1: ON state D_2: ON state	6.21–10.94, 17.22–18.37, 18.76–19.91	6.84–10.64, 17.26–18.35, 18.79–19.90	55.16, 6.46, 5.95	43.48, 6.12, 5.74	Triple-Band X-band, Upper Ku band, Lower K-band
D_1: ON state D_2: OFF state	3.36–4.25, 6.52–13.92, 17.21–8.35, 18.83–19.98	3.28–4.22, 7.01–13.91, 17.25–18.34, 18.84–19.96	23.39, 72.41, 6.41, 5.93	25.07, 65.96, 6.12, 5.77	Quad-Band S band WiMAX, X-band, Upper Ku band, Lower K-band
D_1: OFF state D_2: ON state	3.36–4.25, 6.52–13.92, 17.21–8.35, 18.83–19.98	3.28–4.22, 7.01–13.91, 17.25–18.34, 18.84–19.96	23.39, 72.41, 6.41, 5.93	25.07, 65.96, 6.12, 5.77	Quad-Band S band WiMAX, X-band, Upper Ku band, Lower K-band
D_1: OFF state D_2: OFF state	3.21–6.15, 6.97–12.76, 13.43–14.55, 17.25–18.32, 18.81–19.96	3.20–5.98, 7.10–12.78, 13.51–14.52, 17.34–18.32, 18.86–19.96	62.82, 58.69, 8.01, 6.02, 5.93	60.57, 57.14, 7.21, 5.49, 5.67	Penta-Band S band WiMAX, C band WLAN, 5G NR bands, X-band, Lower Ku band, Lower K band

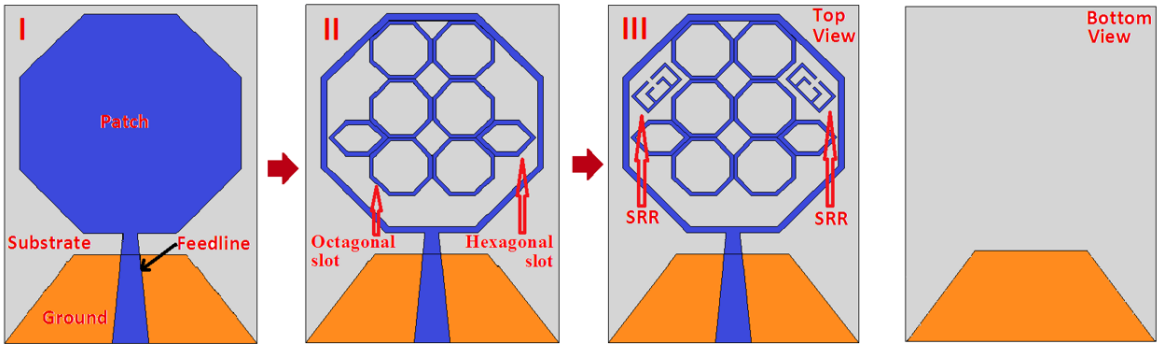

FIGURE 1. Slotted octagonal SRR antenna — Antenna evolution: Configurations I, II, and III.

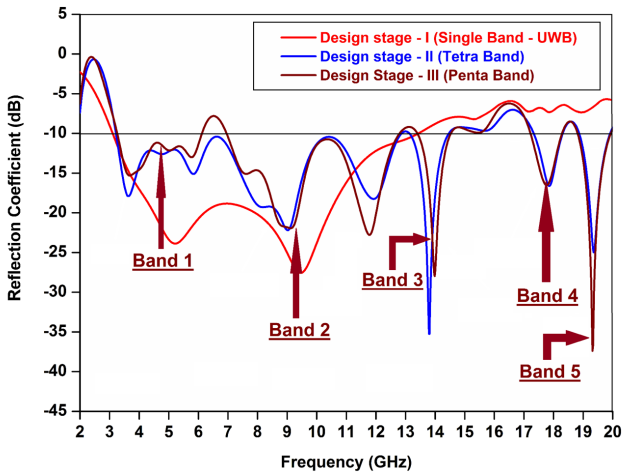

FIGURE 2. Simulated S_{11} of proposed slotted multiband antenna for configurations I, II, and III.

pactness, multiband capability, stable radiation performance, and design flexibility, making it an attractive choice for advanced wireless applications. As shown in Figure 1, the initial design (Stage I) features an octagonal radiating patch fed by a trapezoidal microstrip line, covering an ultra-wideband (UWB) single mode. In Stage II, an octagonal slot with six sections and two hexagonal slotted geometries are introduced within the radiating patch. This modification enables the antenna to resonate at multiple bands: 5.28 GHz [3.24–6.42 GHz (S-band WiMAX, C-band WLAN)], 8.98 GHz [8–12 GHz (X-band)], and 13.78 GHz [13.23–14.66 GHz (Lower Ku-band)], as shown in Figures 1 (Stage II) and 2. The slotted octagonal and hexagonal sections within the radiating patch generate current perturbation, enabling triple-band operation. In Stage III, two SRR (split-ring resonator) cells are integrated into the radiating part, introducing additional resonant bands for wireless standards such as WiMAX, 5G NR bands, WLAN, X-band, Lower Ku-band, Upper Ku-band, and Lower K-band. The SRR cells create a new resonant band at 3.51 GHz (WiMAX: Upper S-band) due to their negative permeability characteristics, which drive solenoidal currents in the SRR rings, leading to a magnetic response. In this final stage, the proposed design achieves

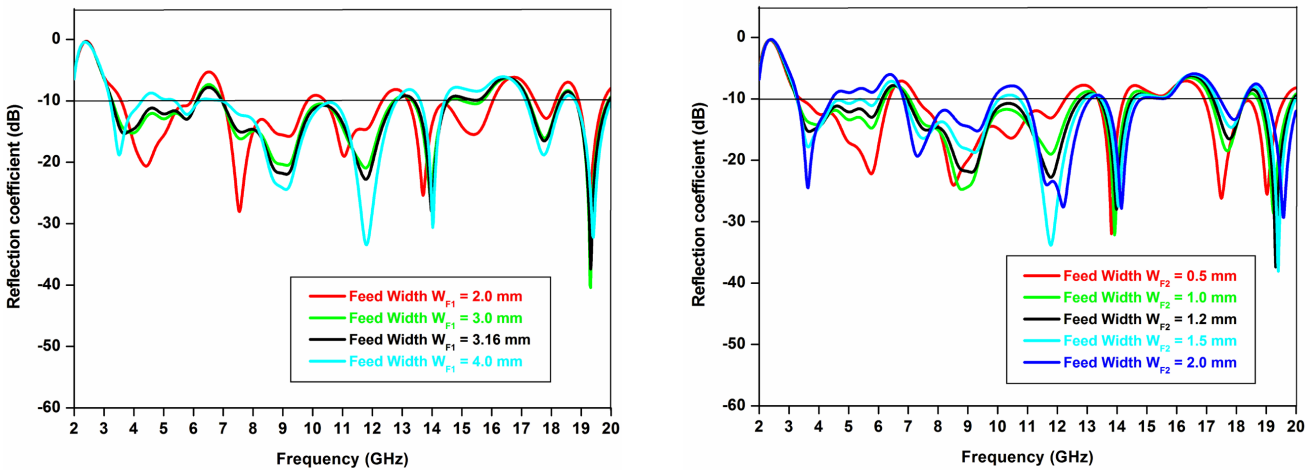

FIGURE 3. Feedline widths parametric analysis.

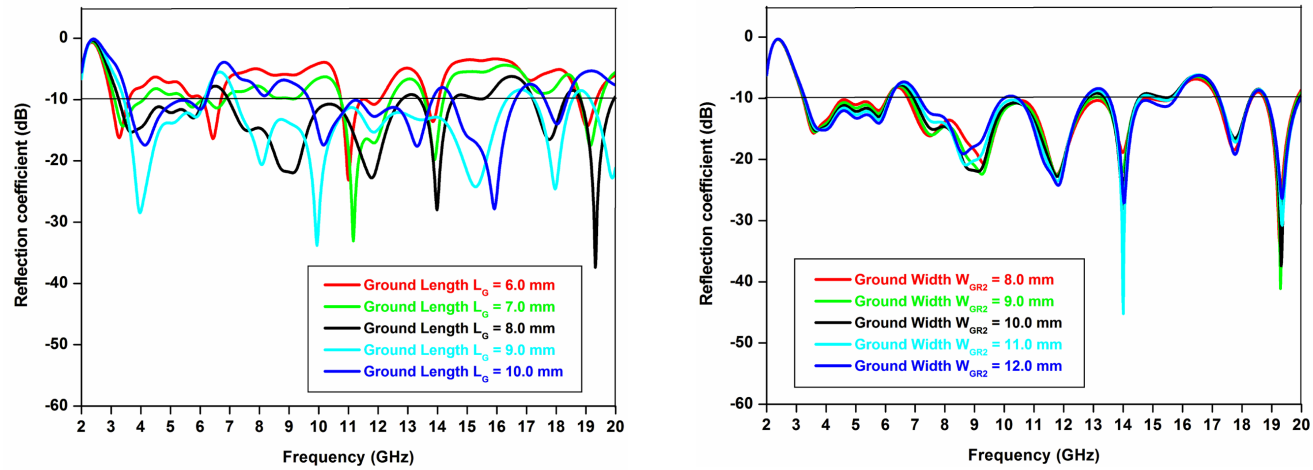

FIGURE 4. Ground dimensions parametric analysis.

a penta-band configuration, covering wireless standards such as S-band WiMAX (3.5 GHz), 5G NR bands (n48, n46, n47, n77, n78, n79), C-band WLAN (5.0/5.8 GHz), X-band (8–12 GHz), Lower Ku-band radar (13.98 GHz), Upper Ku-band molecular rotational spectroscopy (17.76 GHz), and Lower K-band astronomical observations (19.35 GHz), as shown in Figures 1 and 2 (Stage III). The slotted formation and SRR cell integration create current perturbations in the antenna structure, resulting in the penta-band configuration.

The parametric analysis of the proposed slotted metamaterial-inspired multiband antenna reveals that the feedline widths (W_{f1} & W_{f2}) and ground plane dimensions (L_G & W_{GR2}) significantly influence antenna performance. As shown in Figure 3, adjusting the feedline widths (W_{f1} from 2 to 4 mm and W_{f2} from 0.5 to 2 mm) leads to optimal impedance matching (S_{11}) across five operating bands when W_{f1} is set to 3.16 mm and W_{f2} to 1.2 mm. It is also observed that, at lower resonant frequencies (below 9 GHz), reducing the feedline widths enhances S_{11} performance, whereas at higher frequencies (above 10 GHz), increasing the feedline widths improves the impedance matching.

The ground plane dimensions of the antenna are also analyzed to evaluate their effect on performance, particularly with variations in L_G from 6 to 10 mm and W_{GR2} from 8 to 12 mm. Optimized impedance matching (S_{11}) is achieved when the ground length (L_G) is 8 mm and the ground width (W_{GR2}) is 10 mm, as shown in Figure 4. Additionally, varying the ground dimensions helps control the impedance matching across the resonant bands. Increasing both L_G and W_{GR2} generates additional operating bands with improved bandwidth. As depicted in Figure 4, at lower resonant frequencies (below 9 GHz), reducing the ground dimensions enhances impedance matching, while at higher frequencies (above 10 GHz), increasing the ground dimensions improves performance. The optimized antenna performance is thus achieved through careful parametric investigation of feedline widths and ground dimensions.

In design step-II (Figure 1), the proposed antenna incorporates an octagon-shaped slot within the radiating patch, featuring six octagonal and two hexagonal slotted sections arranged in a triple-duplication pattern. This configuration enables the antenna to achieve multiband characteristics, resonating at 5.81, 8.85, 14.24, and 19.31 GHz, as illustrated in Figure 5. The slotted octagonal and hexagonal geometries in-

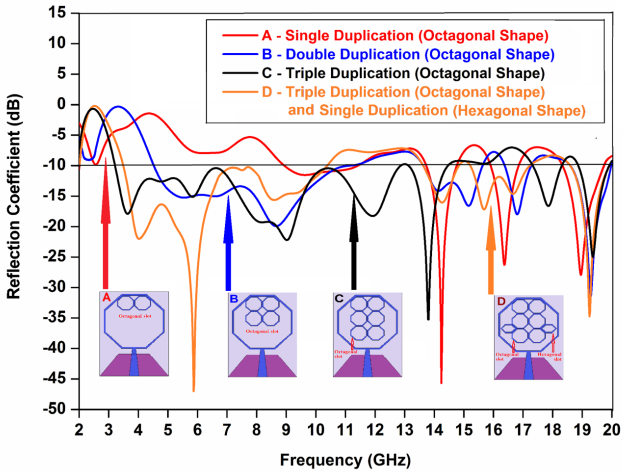

FIGURE 5. Simulated S_{11} for duplication states of the slotted octagonal/hexagonal geometry of the proposed antenna.

duce current perturbation in the antenna, resulting in tetra-band performance. The observed resonant bands cover C-band WLAN (5.0/5.8 GHz), X-band (8–12 GHz for satellite communication, radar, terrestrial broadband, and space communication), Lower Ku-band (13.28–14.68 GHz for radar communication), Upper Ku-band (15.24–17.98 GHz for molecular rotational spectroscopy), and Lower K-band (18.58–19.92 GHz for astronomical observation services).

The analysis of the reflection coefficient for the proposed antenna according to the octagonal and hexagonal shape duplication modes demonstrates improved impedance matching and wider bandwidth at the respective resonant bands in the triple duplication mode, compared to the single and double duplication modes, as illustrated in Figure 5. The simulated results of the proposed design across different duplication modes demonstrate significant variations in resonant frequency ranges, reflection coefficients, and bandwidth performance. For Design A with single duplication, achieved using two octagonal slotted sections, the antenna resonates over four bands: 8.87–11.38 GHz, 13.42–14.58 GHz, 15.98–16.78 GHz, and 18.01–19.87 GHz, with corresponding reflection coefficients of −12.87 dB, −47.32 dB, −26.22 dB, and −28.12 dB. The operating bandwidths obtained for these bands are 24.79%, 8.28%, 4.88%, and 9.82%, respectively. In Design B, double duplication is applied with four octagonal slotted sections. This configuration achieves resonances across 4.41–11.12 GHz, 13.28–15.56 GHz, 16.21–17.34 GHz, and 18.48–19.91 GHz. The reflection coefficients are −21.08 dB, −17.12 dB, −18.78 dB, and −30.06 dB, while the corresponding bandwidths are 91.33%, 13.49%, 5.09%, and 7.85%. With Design C, triple duplication is introduced through six octagonal slotted sections. The resonant frequency bands are 3.48–12.87 GHz, 12.91–14.26 GHz, 17.10–17.98 GHz, and 18.68–19.88 GHz, producing reflection coefficients of −23.42 dB, −36.82 dB, −16.62 dB, and −24.76 dB. The associated bandwidths achieved are 122.72%, 9.39%, 5.97%, and 5.31%, respectively. Finally, Design D extends the triple duplication by combining six octagonal with two hexagonal slotted sections. This design achieves resonances in the ranges of 3.81–10.48 GHz, 13.71–14.68 GHz, 15.24–16.92 GHz, and 18.47–19.89 GHz, with reflection coefficients of −47.67 dB, −16.24 dB, −17.28 dB, and −34.86 dB. The operating bandwidths are 101.91%, 11.49%, 13.19%, and 7.23%, respectively. Figure 6 illustrates the electrical equivalent model of the proposed design, incorporating inductive (L) and capacitive (C) elements to establish resonant characteristics.

As observed in Figure 1, the perimeter of the proposed rectangular SRR is determined by the length and width of the rectangular rings, denoted as L_{SRRI} & L_{SRRE} for the lengths, and W_{SRRI} & W_{SRRE} for the widths, respectively (as depicted in Figure 7).

$$P_{\text{SRRI}} = 2\left(L_{\text{SRRI}} + W_{\text{SRRI}}\right) = \frac{\lambda_g}{2} = \frac{c}{2f_0\sqrt{\varepsilon_{\text{eff}}}} \quad (1)$$

$$P_{\text{SRRE}} = 2\left(L_{\text{SRRE}} + W_{\text{SRRE}}\right) = \frac{\lambda_g}{2} = \frac{c}{2f_0\sqrt{\varepsilon_{\text{eff}}}} \quad (2)$$

$$\varepsilon_{\text{effect}} = 0.5\left(\varepsilon_r + 1\right) + \frac{0.5\left(\varepsilon_r - 1\right)}{\sqrt{1 + \frac{12h_{\text{subst}}}{W_{\text{fln}}}}} \quad (3)$$

Equations (1) and (2) establish the relationship between the SRR perimeter and the guided wavelength (λ_g) at the corresponding resonant frequency (f_0). Equation (3) calculates the effective dielectric constant ($\varepsilon_{\text{effect}}$), which depends on the substrate height (h_{subst}), feedline width (W_{fln}), and the relative permittivity of the substrate (ε_r) [35]. Configuration II (as shown in Figures 1 and 2) demonstrates the antenna's operation at the 3.51 GHz lower resonant frequency band (Upper S band). To introduce additional wireless communication bands, six octagonal and two hexagonal slotted sections with two SRR cells are placed inside the radiating patch area, connected to a trapezoidal feedline (Configuration III: from Figures 1 and 2).

The five excited modes, observed at 3.51, 9.11, 13.98, 17.76, and 19.35 GHz, correspond to distinct eigenvalues. Though each mode is different, they are allocated to their respective wireless standards. Impedance matching for these resonant modes is achieved by the incorporation of the slotted octagonal radiating part and two SRR cells in the design. The input impedance of the proposed structure is determined through analysis of the electromagnetic fields between the radiating patch and the ground plane. Each radiating mode can be modeled by a general parallel resonant RLC circuit, with the equivalent input impedance expressed in Equation (4) [36–39]:

$$(Z_{\text{input}})_{\text{equiv}}(f) = \text{j}\omega L_\infty + \sum_{i=1}^{N} [R_{r,i}/(1+\text{j})Q_{u,i}\{(f/f_{r,i})(f_{r,i}/f)\}] \quad (4)$$

where,

$(Z_{\text{input}})_{\text{equiv}}$ = Equivalent input impedance at feed point of the antenna,
L_∞ = Equivalent Inductance at higher frequency bands,
N = Number of radiating resonant modes,
$f_{r,i}$ = Resonant frequency of the ith mode,
$Q_{u,i}$ = Q-factor of ith resonant mode,

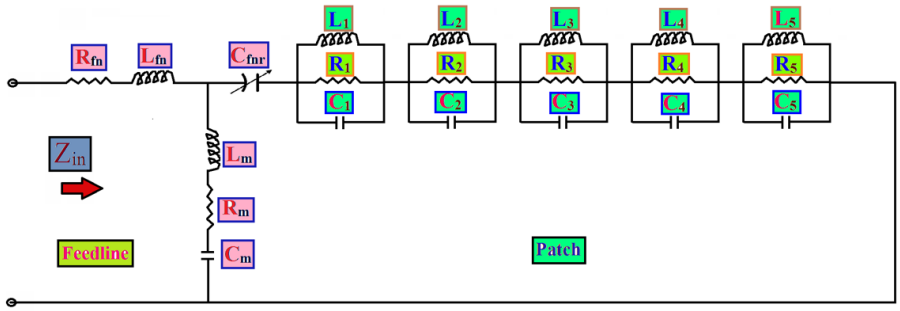

FIGURE 6. Equivalent circuit model for the proposed slotted multiband design.

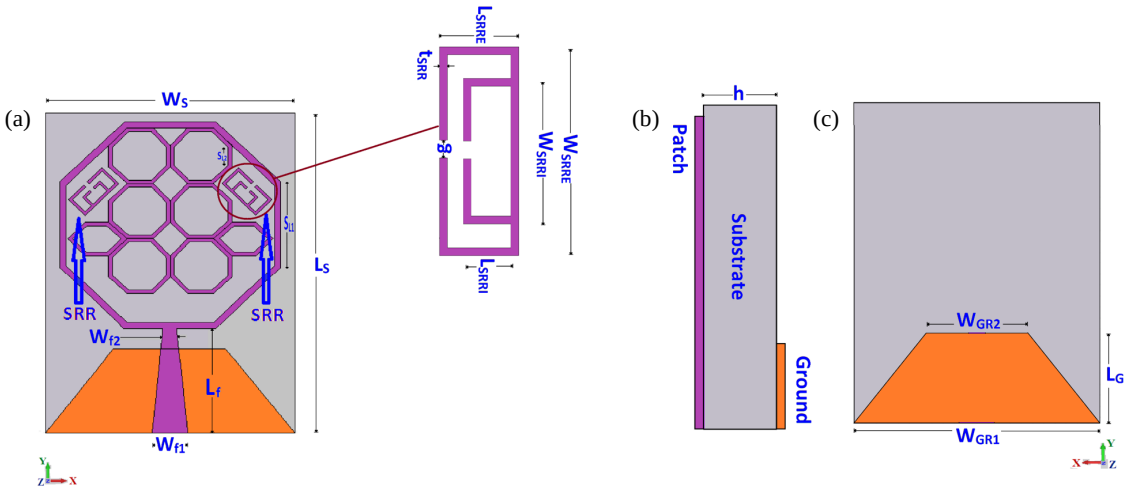

FIGURE 7. Layout of the proposed structure: (a) Top view, (b) side view, (c) bottom view.

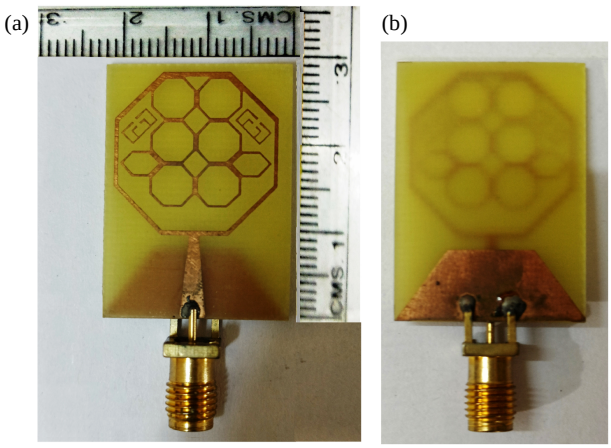

FIGURE 8. Fabricated antenna design: (a) Front side, (b) back side.

$R_{r,i}$ = Radiation resistance of the ith mode, and
$\omega = 2\pi$ (resonant frequency in radian/second).

In design Stage-III, the proposed antenna is fabricated on an FR4 substrate with an electrical size of $0.345\lambda \times 0.257\lambda \times 0.0187\lambda$ (29.5 mm × 22 mm × 1.6 mm) at the lower resonant frequency of 3.51 GHz, featuring a trapezoid-shaped feedline and ground plane, as shown in Figure 7. The radiating section consists of an octagon-shaped slot (side length of 8.0 mm) with six octagonal segments and two hexagonal slotted sections, loaded with two SRR cells. The SRR cells are formed by two rectangular rings, connected at one side and open on the opposite side. The front, side, and back views of the proposed design are presented in Figure 7. The optimized dimensions (in mm) for the antenna design are as follows: $L_S = 29.5$, $W_S = 22$, $h = 1.6$, $S_{L1} = 8$, $S_{L2} = 2$, $L_f = 9.5$, $W_{f1} = 3.16$, $W_{f2} = 1.2$, $W_{GR1} = 22$, $W_{GR2} = 10$ and $L_G = 8$. The antenna was simulated using CST Microwave Studio (MWS) software [40] with the finite element method. After completing the simulation, the design was fabricated using a PCB prototype machine. The fabricated prototype is depicted in Figure 8. The measurement setup, arranged to evaluate the S-parameters (S_{11}), radiation patterns, gain, and efficiency of the proposed design, utilizes a vector network analyzer (VNA) and an anechoic chamber, as illustrated in Figure 9. In the proposed setup, far-field radiation patterns are obtained using a horn antenna as the reference and the proposed antenna as the antenna under test (ATU). These far-field measurements follow the condition $R \gg 2D^2/\lambda$, as dictated by the Friis equation. The radiation pattern of the proposed antenna is recorded in 5° increments, from 0° to 360°, using a turntable, and measured at various resonant frequencies for both co-polarization and cross-polarization modes in the E- and H-planes.

The following steps outline the process for measuring radiation efficiency in the setup:

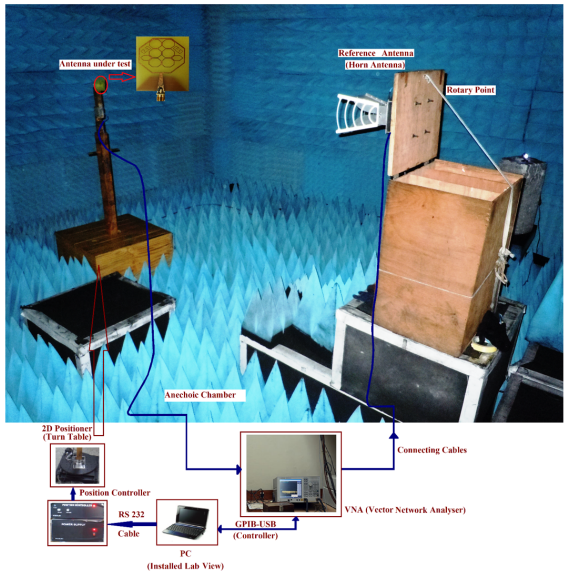

FIGURE 9. Experimental setup: Measurement of various radiation parameters of the proposed antenna.

- Supplied power to the antenna (P_{SUP}): Measured using a power meter.
- Antenna reflection coefficient (Γ): Measured with a vector network analyzer (VNA) connected to the test antenna.
- Accepted power to the antenna (P_{ACP}): Calculated using the equation:

$$P_{\text{ACP}} = \left(1 - |\Gamma|^2\right) \cdot P_{\text{SUP}} \tag{5}$$

- E-field measurement: Performed in 3D at a fixed distance of 1.65 meters.
- Total radiated power (P_{RDP}): Calculated using the equation:

$$P_{\text{RDP}} = \left(r^2/120\pi\right) \sum\nolimits_{i,j} \left(|E_\theta(i,j)|^2 + |E_\Phi(i,j)|^2\right) \sin\theta_i \Delta\theta_i \Delta\Phi_j \tag{6}$$

- Antenna radiation efficiency (η): Calculated as:

$$\eta = P_{\text{RD}}/P_{\text{AC}} \tag{7}$$

This measurement method is also used to determine other antenna parameters, such as S-parameters (reflection coefficient), antenna impedance, radiation patterns, radiation efficiency, and peak gain at different frequencies. Using the same setup, the total radiated power is measured based on the radiated field. However, the field and pattern measurement process can be time-consuming, as it provides 3D results with high uncertainty ($>$ 10%). For very low resonant frequencies, the far-field condition may require a large test site, or a near-field facility can be used for the radiation pattern measurements. In design Stage III, the antenna supports longer current path lengths, leading to penta-band characteristics (Figure 10, Table 3). The antenna demonstrates an $S_{11} < -10$ dB impedance bandwidth of approximately 62.82% (3.21–6.15 GHz), 58.69% (6.97–12.76 GHz), 8.01% (13.43–14.55 GHz), 6.02% (17.25–18.32 GHz), and 5.93% (18.81–19.96 GHz) during simulation. Under experimental testing, the

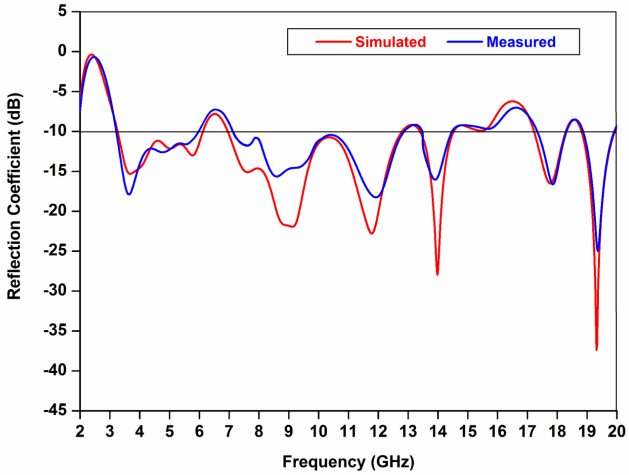

FIGURE 10. Simulated and measured S_{11} results for the proposed multi-band antenna.

corresponding bandwidths are about 60.57% (3.20–5.98 GHz), 57.14% (7.10–12.78 GHz), 7.21% (13.51–14.52 GHz), 5.49% (17.34–18.32 GHz), and 5.67% (18.86–19.96 GHz). The experimental results are obtained using the measurement setup shown in Figure 9. The antenna structure exhibits penta-band resonating characteristics, as illustrated in Figure 10, with the corresponding bandwidth and S-parameter (S_{11}) values. Both the simulated and measured S-parameters (S_{11}) of the proposed structure are also presented in Figure 10. There are discrepancies between the simulated and measured S_{11} results, likely caused by fabrication tolerances and cable losses. Yet, despite these imperfections, the overall agreement is undeniable, confirming the penta-band resonating mode. The impedance matching is optimized, but the lingering mismatch serves as a reminder that precision, even in its best form, is elusive.

The simulated and experimental results of the proposed design show multiple resonating ranges across five distinct bands. In the simulation, the resonating ranges are observed at 3.21–6.15 GHz, 6.97–12.76 GHz, 13.43–14.55 GHz, 17.25–18.32 GHz, and 18.81–19.96 GHz, while the corresponding experimental results demonstrate ranges of 3.20–5.98 GHz, 7.10–12.78 GHz, 13.51–14.52 GHz, 17.34–18.32 GHz, and 18.86–19.96 GHz. The 10-dB bandwidth obtained through simulation is 62.82%, 58.69%, 8.01%, 6.02%, and 5.93% for the respective bands, whereas the experimental analysis yields bandwidth values of 60.57%, 57.14%, 7.21%, 5.49%, and 5.67%. Overall, five resonant bands are achieved. These resonant modes cover a wide range of wireless applications. In the lower frequency region, the design supports S band WiMAX at 3.5 GHz (IEEE 802.16e) and C band WLAN at 5.0/5.8 GHz (IEEE 802.11a/ac). It also complies with several 5G NR bands, including n48 (3.55–3.70 GHz), n46 (5.15–5.925 GHz), n47 (5.855–5.925 GHz), n77 (3.3–4.2 GHz), n78 (3.3–3.8 GHz), and n79 (4.4–5.0 GHz). In the higher frequency spectrum, the antenna supports X-band applications at 9.11 GHz and 11.78 GHz, which are suitable for satellite communication, radar, terrestrial broadband, and space communication. Additionally, it covers the lower Ku band at 13.98 GHz for radar communication, the upper Ku band at 17.76 GHz for molecular

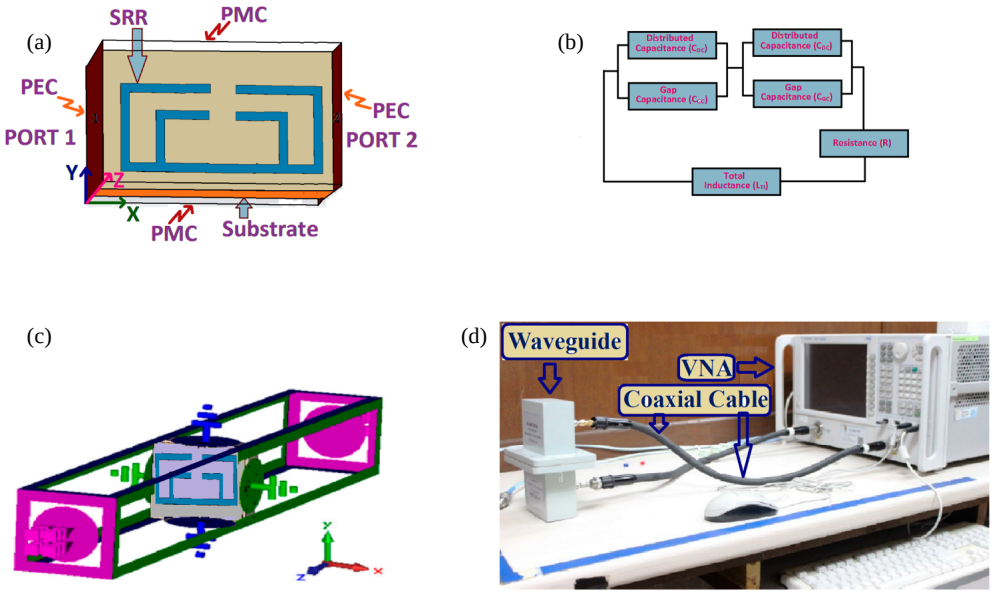

FIGURE 11. (a) Waveguide setup (simulation mode), (b) equivalent circuit, (c) boundary condition representation, and (d) waveguide measurement setup.

rotational spectroscopy, and the lower K band at 19.35 GHz for astronomical observation services.

2.1. Study of Metamaterial SRR

This section presents the design analysis of the proposed metamaterial SRR (Split Ring Resonator) structure, consisting of two modified rectangular metallic rings with split gaps, as shown in Figure 11. Electromagnetic simulation is used to evaluate the fundamental field quantities derived from Maxwell's equations through numerical methods. For accurate analysis and optimized design, proper selection of feeding techniques, structure meshing, and suitable boundary conditions are essential. In the proposed design, CST Microwave Studio is employed as the electromagnetic simulator for numerical investigations, with boundary conditions incorporated to accelerate computation in metamaterial structures [40, 41]. The Perfect Electromagnetic Conductor (PEMC) boundary condition, a generalization of the Perfect Electric Conductor (PEC) and Perfect Magnetic Conductor (PMC), is used in simulations. This condition offers the advantages of reduced cross-sectional dimensions and faster computation times. Specifically, PEC and PMC boundaries are applied along the x-axis and y-axis walls, respectively, while electromagnetic waves are incident along the z-axis, as illustrated in Figures 11(a) and (c). From a circuit perspective, a metamaterial can be modeled as a resonant LC circuit with a defined resonance frequency. In this representation, a metallic strip provides effective inductance, while a gap introduces effective capacitance, characterizing the split-ring resonator (SRR). These passive components receive, store, and dissipate energy within the circuit. Figure 11(b) presents the equivalent circuit model of the proposed metamaterial unit cell. For experimental validation, two rectangular waveguide-to-coaxial adapters are employed. The waveguides are connected to a vector network analyzer (VNA) using semi-rigid coaxial cables and connectors. The fabricated prototype was then positioned between the transmitting and receiving waveguides to measure the reflection and transmission coefficients, as shown in Figure 11(d). A waveguide setup is created in the CST Microwave Studio (MWS) simulator [40] (Figure 11) to obtain the transmission parameter (S_{21}) and reflection parameter (S_{11}). The effective parameters [permeability ($\mu_{\text{effective}}$) and permittivity ($\varepsilon_{\text{effective}}$)] of the proposed SRR cell are derived using the S-parameters (S_{11} and S_{21}) from the waveguide setup. For the experimental waveguide setup, the SRR cell is placed inside the waveguide environment, equipped with two coaxial-to-waveguide adapters and a vector network analyzer (VNA), to measure the S-parameters (S_{11} and S_{21}) [41]. The optimized dimensions (in mm) of the proposed SRR cell are: $L_{\text{SRRE}} = 2.09$, $W_{\text{SRRE}} = 4.17$, $L_{\text{SRRI}} = 1.34$, $W_{\text{SRRI}} = 2.19$, $t_{\text{SRR}} = 0.25$, $g = 0.32$. When an external magnetic H-field is applied, an electromagnetic field (EMF) is induced around the SRR cell, which couples with the two rectangular metallic rings. In this setup, current flows from the outer to the inner ring through a distributed capacitance formed by the spacing between the rings. This arrangement works as an LC resonant circuit, providing a specific operating frequency that can be calculated using Equation (8) [42]:

$$f_{\text{o-srr-str}} = \frac{1}{2\pi\sqrt{(L_{\text{total-eq}})(C_{\text{total-eq}})}} \tag{8}$$

where

$$L_{\text{total-eq}} = 0.0002\Big[\{2(L_{\text{SRRE}} + W_{\text{SRRE}}) - g\} \{\log_e 8(L_{\text{SRRE}} + W_{\text{SRRE}} - 0.5g)/t_{\text{SRR}}\} - \alpha\Big], \tag{9}$$

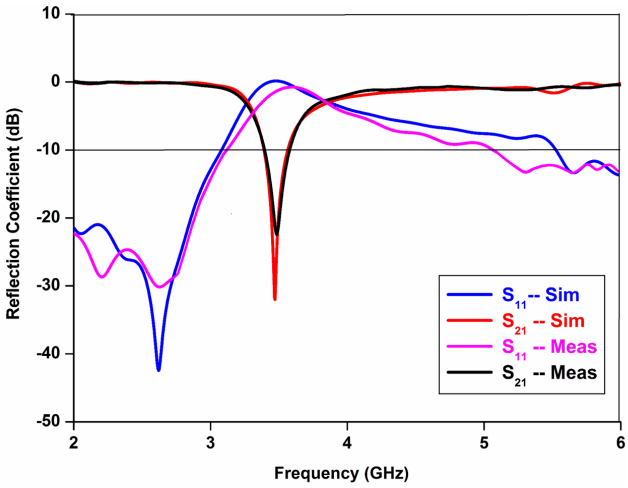

FIGURE 12. Comparison of simulated and measured S_{11} and S_{21} curves.

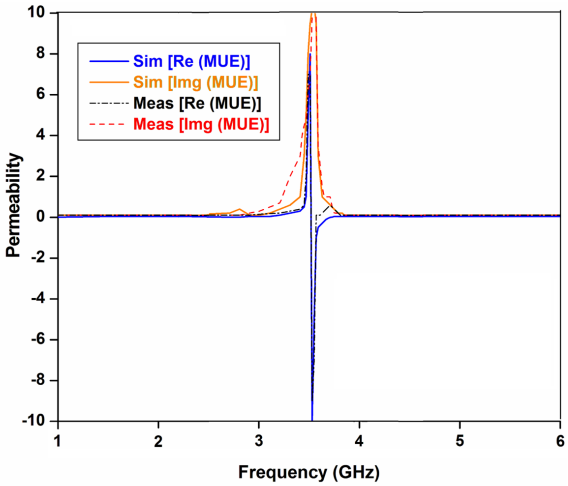

FIGURE 13. Comparison of simulated and measured permeability (real and imaginary mue) curve.

$$C_{\text{total-eq}} = 0.5\Big[\{(L_{\text{SRRE}} + W_{\text{SRRE}}) - \pi(t_{\text{SRR}} + 0.5g) - g\} \{(0.3 \times 10^{-8})(\text{SQRT}(\varepsilon_e))/Z_0\} + \{(8.85 \times 10^{-12})ht_{\text{SRR}}/g\}\Big], \quad (10)$$

where '$L_{\text{total-eq}}$' and '$C_{\text{total-eq}}$' represent the total equivalent inductance and capacitance of the proposed SRR□ 'L_{SRRE}' and 'W_{SRRE}' are the length and width of the external conducting ring□ 'g' is the split gap between the internal and external conducting rings□ and 't_{SRR}' is the thickness of the conducting rings. Constant $\alpha = 2.451$□ 'ε_e' is the effective permittivity of the medium□ 'Z_0' is the characteristic impedance□ and 'h' is the height of the conducting strip.

The effective permeability of the proposed SRR can be calculated using Equation (11) [42, 43]:

$$\mu_{\text{effective-srr-str}} = n_{\text{refractive-ind}} \times z_{\text{imped}} \quad (11)$$

where the refractive index ($n_{\text{refractive-ind}}$) is given by:

$$n_{\text{refractive-ind}} = (1/k^{'}T_{\text{slab}}) \cos^{-1}\left[(1/2S_{21})\left\{1 - (S_{11})^2 + (S_{21})^2\right\}\right] \quad (12)$$

The impedance (z_{imped}) is:

$$z_{\text{imped}} = \left[\left\{(1 + S_{11})^2 - (S_{21})^2\right\} / \left\{(1 - S_{11})^2 - (S_{21})^2\right\}\right]^{1/2} \quad (13)$$

The wave number $k^{'}$ is given by:

$$k^{'} = 2\pi f / \left(3 \times 10^8 \text{ m/s}\right) \quad (14)$$

T_{slab} represents the slab (substrate material) thickness.

Figure 12 illustrates the comparison between the simulated and measured transmission (S_{21}) and reflection (S_{11}) parameters extracted from the waveguide setup. Notably, a transmission peak is observed at the resonant frequency of 3.51 GHz, which aligns with the theoretical value calculated using Equation (8). The proposed SRR structure acts as a magnetic resonator, exhibiting negative permeability characteristics at 3.51 GHz due to the orthogonally induced magnetic field. As shown in Figure 12, the reflection parameter S_{11} hovers near the zero level (below -2 dB), while the transmission parameter S_{21} falls below the -10 dB level at the resonant frequency of 3.51 GHz, indicating stop-band characteristics. This stop-band behavior further confirms the negative permeability nature of the SRR at the 3.51 GHz resonant frequency (Figure 13).

3. RESULTS AND DISCUSSION

The operational mechanism of the proposed design can be better understood by analyzing the simulated surface current distribution at various wireless standard frequencies: 3.51 GHz (S band — WiMAX), 5.75 GHz (C band — WLAN), 9.11 GHz, 11.78 GHz (X band), 13.98 GHz (Lower Ku-band), 17.76 GHz (Upper Ku-band), and 19.35 GHz (Lower K-band), as depicted in Figure 14. At the lower resonant frequency (3.51 GHz, S band — WiMAX), the strongest current distribution is concentrated along the surface of the proposed SRR cells. For the higher frequency (5.75 GHz, C band — WLAN), the surface current distribution is primarily concentrated around the periphery of the slotted radiating patch section connected to the feedline. At even higher frequencies (9.11 GHz and 11.78 GHz in the X band, 13.98 GHz in the Lower Ku-band, 17.76 GHz in the Upper Ku-band, and 19.35 GHz in the Lower K-band), the surface current spreads extensively across the slotted octagonal radiating part with triple-duplicated octagonal and hexagonal sections, leading to wider bandwidth and improved impedance matching. A notable observation is that at the upper X band (11.78 GHz) and Lower Ku-band (13.98 GHz) frequencies, the current density is much denser around the center of the triple-duplicated octagonal structure (attached to the radiating patch) and the trapezoid-shaped feedline. The analysis also shows minimal current around the edges of the two SRR cells and the double hexagonal radiating sections, while the current is

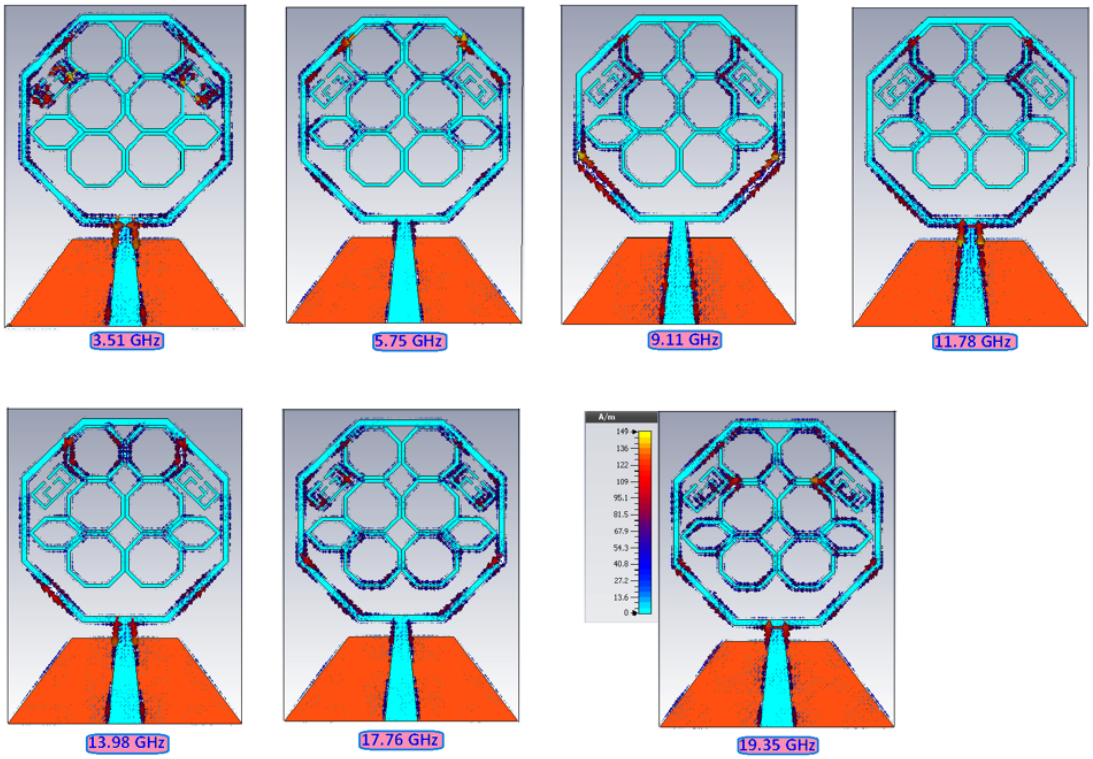

FIGURE 14. Current distribution (in simulation mode) for proposed design at 3.51/5.75/9.11/11.78/13.98/17.76/19.35.

more uniformly distributed across the radiating area. This uniform distribution improves the radiation characteristics, bandwidth, and impedance matching of the antenna. Since the patch length is approximately half of the wavelength at resonance, it behaves as a low-impedance microstrip line with an open circuit at each end. At these open ends, electric field anti-nodes and magnetic nodes are present, representing maximum electric field and minimal magnetic field values, respectively. These fields alternate between positive and negative values. At the center of the patch, there is an electric field node and a magnetic anti-node, with zero electric field and alternating high magnetic field. Another observation is that the surface electric current density (J_S, under the patch) is equivalent to the magnetic field (H, around the patch). Radiation from the patch is produced by two magnetic dipoles formed at the dielectric gaps at the open ends. Displacement current [e (dE/dt)] enhances the magnetic dipole field strength, and these dipoles are most effective along the length of each slot, operating in-phase. Radiation at the open circuit ends is minimal due to the opposing phase of electric currents beneath the patch and on the ground plane. The patch behaves like a series resonant circuit with a capacitor to ground at each end (the gaps) and an inductor in the center. The thicker the substrate and the narrower the patch, the smaller the capacitors and larger the inductance, resulting in higher impedance at the patch edges. At resonance, the radiating patch shows high impedance at the edges, with maximum current distribution at the center [44–47]. The proposed antenna structure achieves peak gains of 2.24, 1.29, 3.32, 3.38, 3.72, 3.21, and 4.38 dBi under simulation, and 1.98, 1.12, 2.98, 3.31, 3.02, 2.86, and 3.98 dBi under measurement at resonant frequencies of 3.51, 5.75, 9.11, 11.78, 13.98, 17.76, and 19.35 GHz, respectively, as shown in Figure 17.

The reduction in antenna gain at lower frequencies is attributed to several factors:

- The slotted octagonal resonator in the design serves as the radiating component, but the inclusion of slotted octagonal and hexagonal geometries reduces the effective radiating patch area. This results in decreased antenna radiation performance, impacting parameters such as gain, radiation efficiency, and polarization. While the slotted geometry enables operation across multiple wireless standards, it also shrinks the active radiating section, leading to a reduction in gain at lower frequencies. However, despite this reduction, the antenna still exhibits acceptable gain at these bands.
- Another factor is the sudden drop in gain in non-resonant frequency regions, as shown in Figure 15. This is caused by stop-band effects present in those regions. The combination of reduced active radiating area and stop-band effects further contributes to the decrease in gain at lower frequency resonant modes.

In contrast, the antenna achieves improved peak gain at higher frequency bands than lower bands. At higher resonant frequencies, the radiating patch dimensions are relatively larger in relation to the wavelength, leading to enhanced gain. Any deviation in measured gain is likely due to measurement errors, which can be minimized by using precise measurements in an anechoic chamber.

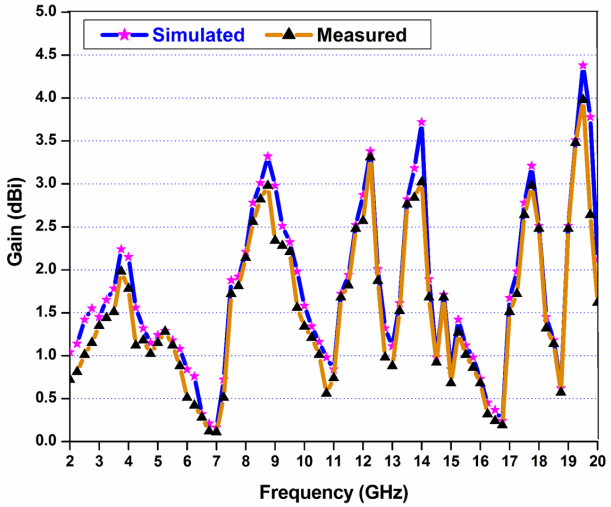

FIGURE 15. Simulated and measured peak gain analysis for the proposed multiband antenna.

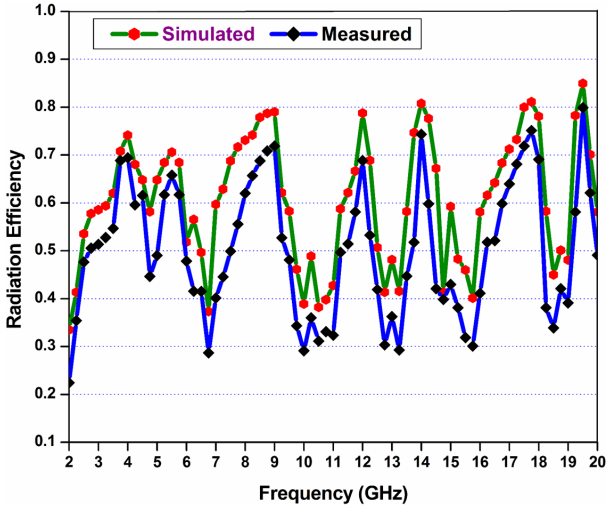

FIGURE 16. Simulated and measured radiation efficiency analysis for the proposed multiband antenna.

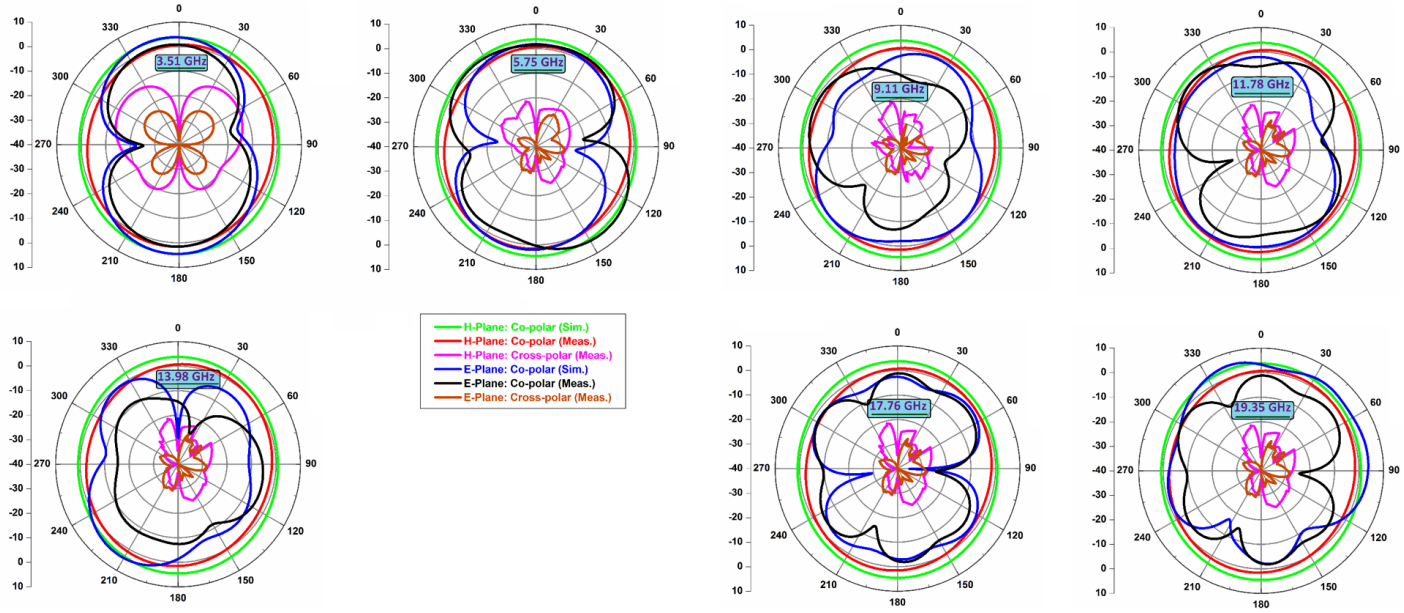

FIGURE 17. E & H plane patterns (co/cross-polarization mode) of the proposed design at 3.51/5.75/9.11/11.78/13.98/17.76/19.35 GHz.

The radiation efficiency of the proposed design is also analyzed in both simulation and measurement modes, as depicted in Figure 16. The design achieves radiation efficiencies of 62.07%, 68.42%, 74.18%, 78.76%, 80.78%, 81.12%, and 84.98% in simulation, and 54.68%, 61.69%, 65.71%, 68.82%, 74.36%, 75.14%, and 79.89% during experimentation, at resonant frequencies of 3.51, 5.75, 9.11, 11.78, 13.98, 17.76, and 19.35 GHz, respectively.

The radiation pattern study further enhances the understanding of the proposed design. Simulated and experimental E and H plane patterns have been analyzed in both co- and cross-polarization modes, showing a strong correlation between the two. As illustrated in Figure 17, the comparison of these patterns at distinct resonant frequencies (3.51, 5.75, 9.11, 11.78, 13.98, 17.76, and 19.35 GHz) reveals that the E-plane patterns resemble a dipole-like or bi-directional radiation, while the H-plane patterns are omnidirectional in co-polarization mode. These characteristics validate the suitability of the design for wireless communication applications. Additionally, it is observed that the radiation patterns remain stable and consistent, with low levels of cross-polarization (below -15 dB) across all resonant frequencies, confirming the design's reliability for multiband operation [48–51].

Table 2 provides a performance comparison between the proposed slotted multiband antenna and several reported antennas. The results demonstrate that the proposed design offers reduced dimensions, enhanced operating bandwidth, and improved gain and efficiency. By utilizing a metamaterial loading approach, the design achieves multiband functionality while delivering superior radiation characteristics compared to previously reported antennas of similar size.

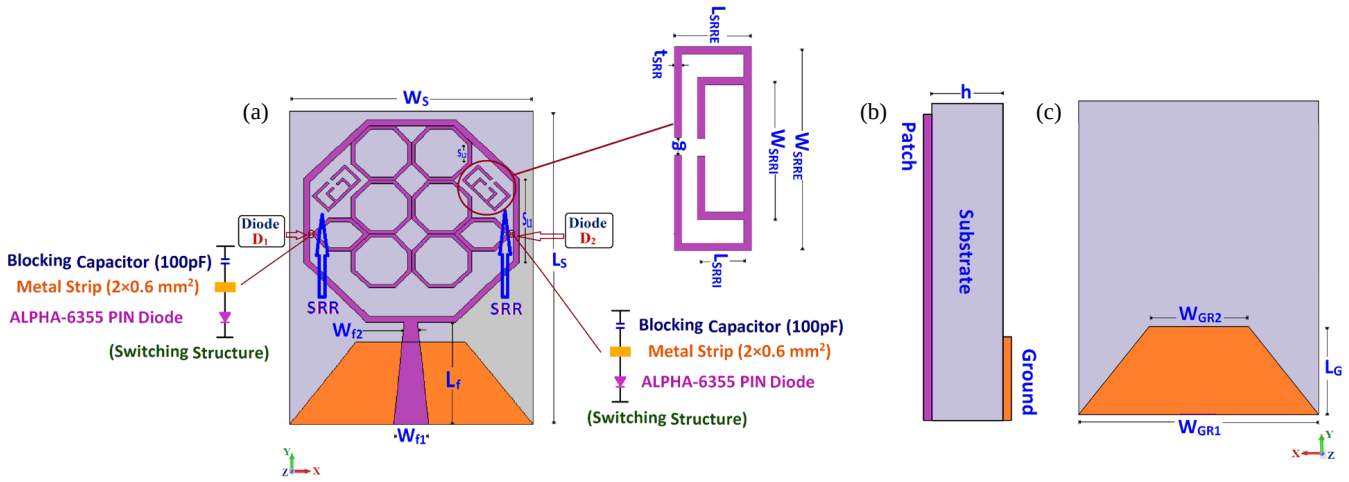

FIGURE 18. (a) Upper view, (b) side view, (c) back view of the proposed design with switching element PIN diode configuration.

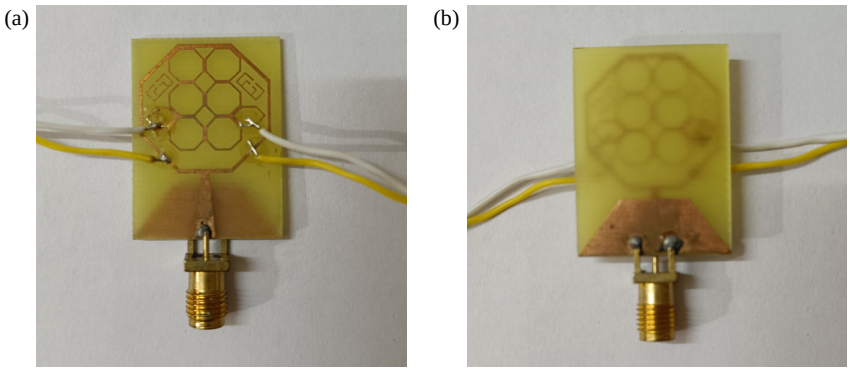

FIGURE 19. Constructed antenna prototype: (a) Front section, (b) rear section.

4. FREQUENCY RECONFIGURABLE CHARACTERISTICS

This section explores the design of the proposed antenna, focusing on its ability to switch between different wireless standards using a PIN diode as a switching element, demonstrating its reconfigurability. The PIN diode is positioned in the gap between the hexagon-shaped slotted radiating section and the outer octagonal geometry of the patch, as illustrated in Figures 18 and 19. This gap is critical in altering the resonant characteristics of the antenna. By changing the biasing states (forward/reverse) of the PIN diode, the gap varies, causing a current perturbation effect, which is key to enabling frequency band reconfiguration. Adjusting the gap between the slotted hexagonal radiating part and the octagonal patch section helps modify the resonant properties of the design, allowing for improved response and the creation of an additional resonant band for wireless communication applications, as summarized in Table 3.

The experimental analysis utilizes ALPHA-6355 beam lead PIN diodes, chosen for their exceptionally low capacitance characteristics [61]. The diode's biasing (ON/OFF mode) is controlled by applying a DC voltage of 0.7 volts. The electrical equivalent model of the diode consists of components $R_{\mathrm{CCF}} = 2.6\,\Omega$ and $R_{\mathrm{CCR}} = 5\,\mathrm{k}\Omega$, connected in series and parallel, along with $L_{\mathrm{FR}} = 0.6\,\mathrm{nH}$ and $C_{\mathrm{RE}} = 0.081\,\mathrm{pF}$, as shown in Figures 20(a) and (b).

To ensure proper operation, a certain degree of isolation must be maintained between the low-frequency DC bias circuit and the RF circuit. Figure 20(c) illustrates the biasing circuit configuration for the ALPHA-6355 beam-lead PIN diode. An RF choke inductor is connected in series with the bias line, while RF bypass capacitors are placed in parallel with the power supply to prevent DC leakage into the RF section. This arrangement provides at least 20 dB of DC/RF isolation. The biasing network consists of two 0.12 pF capacitors acting as DC blocks, two 1 µH inductors serving as RF isolators, and is powered by a regulated 0.7 V supply. In the RF frequency range, the PIN diode behaves as a variable resistor; however, its ON and OFF states exhibit distinct circuit behaviors. Figures 20(a) and (b) depict the equivalent circuits for these states. In the ON state, the diode is modeled as a series RL circuit, comprising an inductor (L) and resistor (R). In the OFF state, it behaves as a parallel RLC circuit, where the inductor is connected to a resistor (R) and capacitor (C) in parallel. The low resistance (R) in the ON-state RL circuit allows current flow between the radiating elements, whereas the high impedance (RLC) configuration in the OFF state restricts current flow, effectively isolating the sections. For simulation simplicity, the PIN diode was modeled as an RL circuit with a constant inductance (L). The resistance

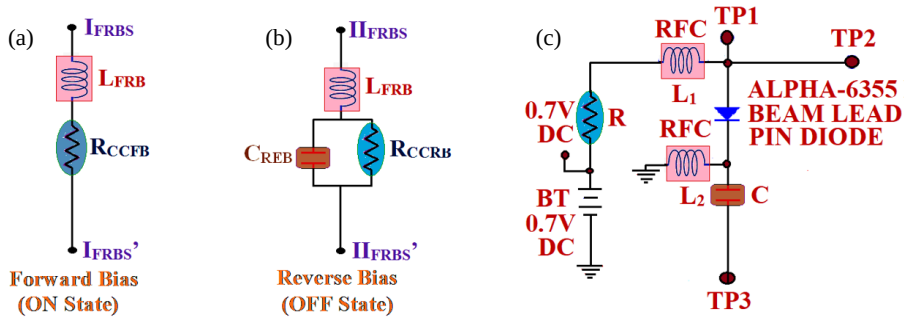

FIGURE 20. Equivalent model and biasing circuit: PIN diode. (a) Forward bias, (b) reverse bias, and (c) biasing circuit.

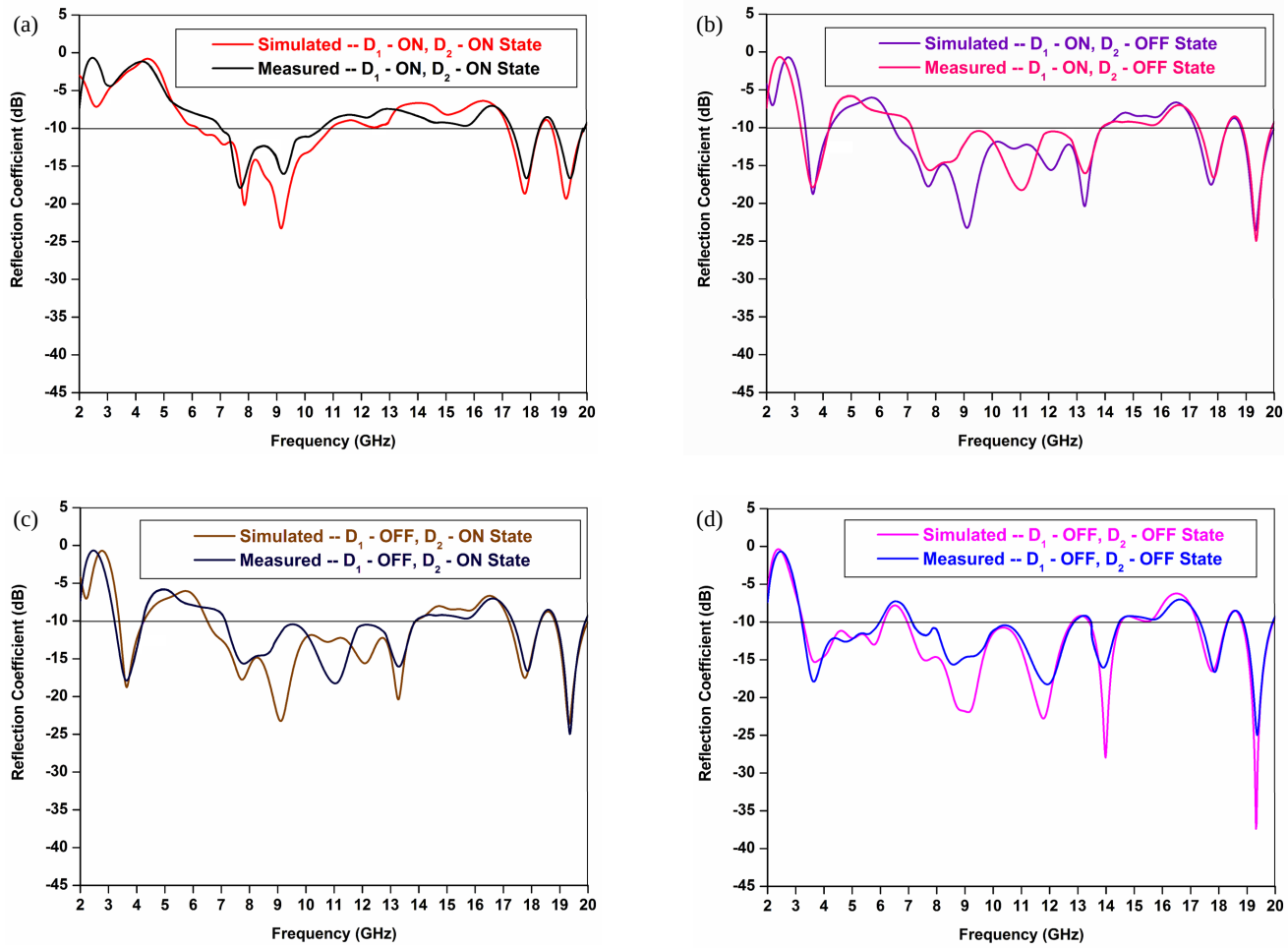

FIGURE 21. Frequency reconfiguration: (a) Mode-I (D_1 — ON, D_2 — ON State), (b) Mode-I (D_1 — ON, D_2 — OFF State), (c) Mode-I (D_1 — OFF, D_2 — ON State), (d) Mode-I (D_1 — OFF, D_2 — OFF State).

(R) was set to 2.6 Ω for the ON state and 5 kΩ for the OFF state. A bias voltage of 0.7 V was applied to achieve the switching conditions between the ON and OFF states.

The tunability across various wireless standards is accomplished by altering the states of the PIN diode, as detailed in Table 3. When the PIN diode is in the ON state, the gap between the slotted hexagonal radiating section and the octagonal slotted geometry is bridged, facilitating the support of additional frequency bands for wireless communication applications (according to the respective states outlined in Table 3). In the OFF state of both PIN diodes, the antenna achieves penta-band characteristics, providing coverage for multiple wireless communication applications (based on the reverse bias state of both diodes as shown in Table 3).

The comparative graphs of the S-parameter (S_{11}) for both simulation and experimental modes are shown in Figure 21. The simulated data is obtained using CST Microwave Studio (MWS) software [40], considering the different PIN diode states as outlined in Table 3. In practice, the operation of the PIN diode requires a biasing circuit to apply forward or reverse

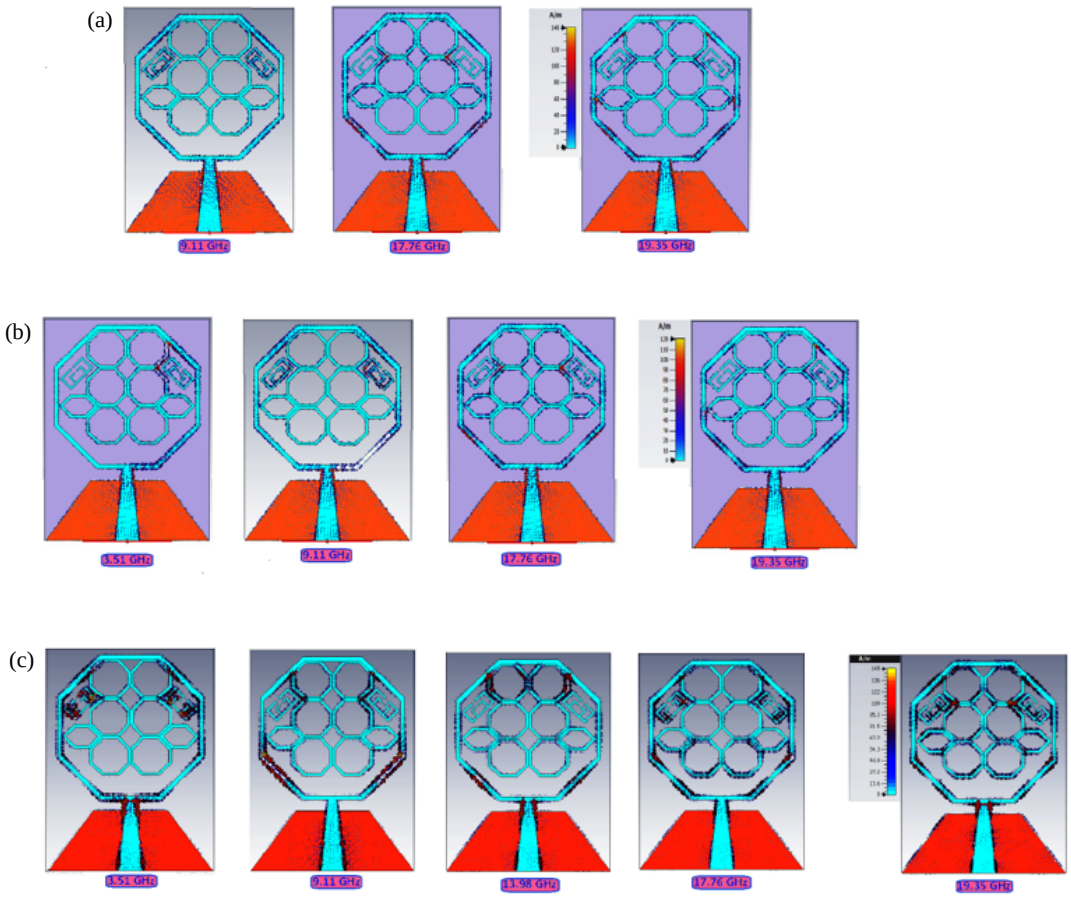

FIGURE 22. Surface current distribution: (a) Diode D_1 and D_2 — ON state, (b) Diode D_1 — ON state and Diode D_2 — OFF state or Diode D_1 — OFF state and Diode D_2 — ON state, and (c) Diode D_1 and D_2 — OFF state.

bias, which may result in minor deviations between the simulated and measured results.

Figure 22 illustrates the effective surface current distribution for all possible switching states of the antenna. The distribution highlights the radiating strength of the different antenna strips and the influence of the introduced slots. The PIN diodes facilitate transitions between high-impedance and low-impedance states over specific current-carrying regions of the structure. Consequently, the passive lumped L-C network undergoes variation through different series and parallel combinations corresponding to the various PIN diode switching configurations. In Figure 22(a), when both D_1 and D_2 are in the ON state (forward bias), a strong and continuous surface current is observed across the entire radiating structure, particularly along the slots and feed region. This indicates effective coupling between the radiating elements, supporting the triple-band operation in the X-, upper Ku-, and lower K-bands. In Figure 22(b), when one diode is ON, and the other is OFF, the surface current becomes partially disrupted in one of the radiating paths while remaining concentrated along the active arm. This asymmetrical current distribution alters the electrical length of the antenna, resulting in quad-band operation covering S-, X-, Ku-, and K-bands. The comparable current distribution for both D_1 ON/D_2 OFF and D_1 OFF/D_2 ON states confirms that either configuration provides a similar frequency response. Finally, in Figure 22(c), with both diodes in the OFF state (reverse bias), the current distribution becomes localized mainly around the feed and slot boundaries. The suppression of current flow between certain sections introduces multiple resonant paths, leading to the penta-band configuration. This state exhibits distinct current loops corresponding to S-, C-, X-, Ku-, and K-band resonances, demonstrating the successful reconfigurability of the antenna design.

5. CONCLUSION

A frequency reconfigurable metamaterial-inspired slotted multiband antenna is designed and analyzed, incorporating a PIN diode, SRR cells and slotted octagonal/hexagonal structures, for various wireless standards, including S band WiMAX (3.5 GHz), C band WLAN (5.0/5.8 GHz), X band (9.17 GHz, 11.8 GHz) for Satellite communication, radar, terrestrial broadband, space communication applications, Lower Ku band (14.01 GHz) for radar communication application, Upper Ku band (17.81 GHz) for molecular rotational spectroscopy, and Lower K band (19.40 GHz) for astronomical observation services. The antenna features a radiating patch with six octagonal and two hexagonal slotted sections, along with metamaterial-inspired SRR cells to achieve penta-band functionality. The achieved frequency-band reconfigurability for wireless standards is facilitated by the PIN diode acting as the switching element. The design demonstrates

stable and consistent E & H plane patterns with low cross-polarization, acceptable gain and radiation efficiency, and improved impedance matching across the operating wireless communication bands.

ACKNOWLEDGEMENT

The author expresses gratitude to Prof. S. K. Koul of CARE, IIT Delhi, India, for generously providing measurement facilities.

REFERENCES

[1] Elsheakh, D. M. N., H. Elsadek, E. Abdallah, M. F. Iskander, and H. El-Hennawy, "Reconfigurable single and multiband inset feed microstrip patch antenna for wireless communication devices," *Progress In Electromagnetics Research C*, Vol. 12, 191–201, 2010.

[2] Bakariya, P. S., S. Dwari, M. Sarkar, and M. K. Mandal, "Proximity-coupled microstrip antenna for Bluetooth, WiMAX, and WLAN applications," *IEEE Antennas and Wireless Propagation Letters*, Vol. 14, 755–758, 2015.

[3] Wu, R.-Z., P. Wang, Q. Zheng, and R.-P. Li, "Compact CPW-fed triple-band antenna for diversity applications," *Electronics Letters*, Vol. 51, No. 10, 735–736, 2015.

[4] Mehdipour, A., A.-R. Sebak, C. W. Trueman, and T. A. Denidni, "Compact multiband planar antenna for 2.4/3.5/5.2/5.8-GHz wireless applications," *IEEE Antennas and Wireless Propagation Letters*, Vol. 11, 144–147, 2012.

[5] Cao, Y. F., S. W. Cheung, and T. I. Yuk, "A multiband slot antenna for GPS/WiMAX/WLAN systems," *IEEE Transactions on Antennas and Propagation*, Vol. 63, No. 3, 952–958, 2015.

[6] Saraswat, R. K. and M. Kumar, "A frequency band reconfigurable UWB antenna for high gain applications," *Progress In Electromagnetics Research B*, Vol. 64, 29–45, 2015.

[7] Samsuzzaman, M., T. Islam, N. H. A. Rahman, M. R. I. Faruque, and J. S. Mandeep, "Compact modified Swastika shape patch antenna for WLAN/WiMAX applications," *International Journal of Antennas and Propagation*, Vol. 2014, No. 1, 825697, 2014.

[8] Ali, T., M. M. Khaleeq, S. Pathan, and R. C. Biradar, "A multiband antenna loaded with metamaterial and slots for GPS/WLAN/WiMAX applications," *Microwave and Optical Technology Letters*, Vol. 60, No. 1, 79–85, 2018.

[9] Chaurasia, P., B. K. Kanaujia, S. Dwari, and M. K. Khandelwal, "Design and analysis of seven-bands-slot-antenna with small frequency ratio for different wireless applications," *AEU — International Journal of Electronics and Communications*, Vol. 99, 100–109, 2019.

[10] Zhu, J. and G. V. Eleftheriades, "Dual-band metamaterial-inspired small monopole antenna for WiFi applications," *Electronics Letters*, Vol. 45, No. 22, 1104–1106, 2009.

[11] Xu, H.-X., G.-M. Wang, Y.-Y. Lv, M.-Q. Qi, X. Gao, and S. Ge, "Multifrequency monopole antennas by loading metamaterial transmission lines with dual-shunt branch circuit," *Progress In Electromagnetics Research*, Vol. 137, 703–725, 2013.

[12] Alam, T., M. Samsuzzaman, M. R. I. Faruque, and M. T. Islam, "A metamaterial unit cell inspired antenna for mobile wireless applications," *Microwave and Optical Technology Letters*, Vol. 58, No. 2, 263–267, 2016.

[13] Daniel, R. S., R. Pandeeswari, and S. Raghavan, "A compact metamaterial loaded monopole antenna with offset-fed microstrip line for wireless applications," *AEU — International Journal of Electronics and Communications*, Vol. 83, 88–94, 2018.

[14] Rao, M. V., B. T. P. Madhav, T. Anilkumar, and B. P. Nadh, "Metamaterial inspired quad band circularly polarized antenna for WLAN/ISM/Bluetooth/WiMAX and satellite communication applications," *AEU — International Journal of Electronics and Communications*, Vol. 97, 229–241, 2018.

[15] Anguera, J., C. Puente, C. Borja, and J. Soler, "Fractal shaped antennas: A review," *Encyclopedia of RF and Microwave Engineering*, Wiley, 2005.

[16] Chen, H.-D., H.-W. Yang, and C.-Y.-D. Sim, "Single open-slot antenna for LTE/WWAN smartphone application," *IEEE Transactions on Antennas and Propagation*, Vol. 65, No. 8, 4278–4282, 2017.

[17] Lee, S. H., Y. Lim, Y. J. Yoon, C.-B. Hong, and H.-I. Kim, "Multiband folded slot antenna with reduced hand effect for handsets," *IEEE Antennas and Wireless Propagation Letters*, Vol. 9, 674–677, 2010.

[18] Yuan, B., Y. Cao, and G. Wang, "A miniaturized printed slot antenna for six-band operation of mobile handsets," *IEEE Antennas and Wireless Propagation Letters*, Vol. 10, 854–857, 2011.

[19] Sharma, S. K., J. D. Mulchandani, D. Gupta, and R. K. Chaudhary, "Triple-band metamaterial-inspired antenna using FDTD technique for WLAN/WiMAX applications," *International Journal of RF and Microwave Computer-Aided Engineering*, Vol. 25, No. 8, 688–695, 2015.

[20] Ali, T. and R. C. Biradar, "A compact multiband antenna using $\lambda/4$ rectangular stub loaded with metamaterial for IEEE 802.11N and IEEE 802.16E," *Microwave and Optical Technology Letters*, Vol. 59, No. 5, 1000–1006, 2017.

[21] Kukreja, J., D. K. Choudhary, and R. K. Chaudhary, "CPW fed miniaturized dual-band short-ended metamaterial antenna using modified split-ring resonator for wireless application," *International Journal of RF and Microwave Computer-Aided Engineering*, Vol. 27, No. 8, e21123, 2017.

[22] Saraswat, R. K. and M. Kumar, "A metamaterial hepta-band antenna for wireless applications with specific absorption rate reduction," *International Journal of RF and Microwave Computer-Aided Engineering*, Vol. 29, No. 10, e21824, 2019.

[23] Ali, T., M. S. Aw, and R. C. Biradar, "A fractal quad-band antenna loaded with L-shaped slot and metamaterial for wireless applications," *International Journal of Microwave and Wireless Technologies*, Vol. 10, No. 7, 826–834, 2018.

[24] Pandeeswari, R. and S. Raghavan, "Broadband monopole antenna with split ring resonator loaded substrate for good impedance matching," *Microwave and Optical Technology Letters*, Vol. 56, No. 10, 2388–2392, 2014.

[25] Arora, C., S. S. Pattnaik, and R. N. Baral, "SRR inspired microstrip patch antenna array," *Progress In Electromagnetics Research C*, Vol. 58, 89–96, 2015.

[26] Rajeshkumar, V. and S. Raghavan, "SRR-based polygon ring penta-band fractal antenna for GSM/WLAN/WiMAX/ITU band applications," *Microwave and Optical Technology Letters*, Vol. 57, No. 6, 1301–1305, 2015.

[27] Elavarasi, C. and T. Shanmuganantham, "Multiband SRR loaded Koch star fractal antenna," *Alexandria Engineering Journal*, Vol. 57, No. 3, 1549–1555, 2018.

[28] Ahmad, B. H. and H. Nornikman, "Fractal microstrip antenna with Minkowski island split ring resonator for broadband application," in *2013 IEEE International RF and Microwave Conference (RFM)*, 214–218, Penang, Malaysia, 2013.

[29] Hu, J.-R. and J.-S. Li, "Compact microstrip antennas using CSRR structure ground plane," *Microwave and Optical Technology Letters*, Vol. 56, No. 1, 117–120, 2014.

[30] Rajkumar, R. and K. U. Kiran, "A metamaterial inspired compact open split ring resonator antenna for multiband operation," *Wireless Personal Communications*, Vol. 97, No. 1, 951–965, 2017.

[31] Rajeshkumar, V. and S. Raghavan, "A compact metamaterial inspired triple band antenna for reconfigurable WLAN/WiMAX applications," *AEU — International Journal of Electronics and Communications*, Vol. 69, No. 1, 274–280, 2015.

[32] Saraswat, R. K. and M. Kumar, "A vertex-fed hexa-band frequency reconfigurable antenna for wireless applications," *International Journal of RF and Microwave Computer-Aided Engineering*, Vol. 29, No. 10, e21893, 2019.

[33] Liu, W.-C., C.-M. Wu, and Y. Dai, "Design of triple-frequency microstrip-fed monopole antenna using defected ground structure," *IEEE Transactions on Antennas and Propagation*, Vol. 59, No. 7, 2457–2463, 2011.

[34] Saraswat, R. K. and M. Kumar, "Miniaturized slotted ground UWB antenna loaded with metamaterial for WLAN and WiMAX applications," *Progress In Electromagnetics Research B*, Vol. 65, 65–80, 2016.

[35] Balanis, C. A., *Antenna Theory: Analysis and Design*, John Wiley & Sons, 2005.

[36] Saraswat, R. K. and M. Kumar, "Implementation of metamaterial loading to miniaturized UWB dipole antenna for WLAN and WiMAX applications with tunability characteristics," *IETE Journal of Research*, Vol. 68, No. 3, 2022–2035, 2022.

[37] Naqvi, S. A. and M. S. Khan, "Design of a miniaturized frequency reconfigurable antenna for rectenna in WiMAX and ISM frequency bands," *Microwave and Optical Technology Letters*, Vol. 60, No. 2, 325–330, 2018.

[38] Li, W., Y. Liu, J. Li, L. Ye, and Q. H. Liu, "Modal proportion analysis in antenna characteristic mode theory," *International Journal of Antennas and Propagation*, Vol. 2019, No. 1, 7069230, 2019.

[39] Garg, R., P. Bhartia, and I. Bahl, *Microstrip Antenna Design Handbook*, Artech House, Boston, MA, USA, 2001.

[40] Computer simulation technology microwave studio (CST MWS), retrieved from http://www.cst.co.

[41] Chen, H., J. Zhang, Y. Bai, Y. Luo, L. Ran, Q. Jiang, and J. A. Kong, "Experimental retrieval of the effective parameters of metamaterials based on a waveguide method," *Optics Express*, Vol. 14, No. 26, 12 944–12 949, 2006.

[42] Saha, C. and J. Y. Siddiqui, "Versatile CAD formulation for estimation of the resonant frequency and magnetic polarizability of circular split ring resonators," *International Journal of RF and Microwave Computer-Aided Engineering*, Vol. 21, No. 4, 432–438, 2011.

[43] Smith, D. R., S. Schultz, P. Markoš, and C. M. Soukoulis, "Determination of effective permittivity and permeability of metamaterials from reflection and transmission coefficients," *Physical Review B*, Vol. 65, No. 19, 195104, 2002.

[44] Agrawal, A., P. K. Singhal, and A. Jain, "Design and optimization of a microstrip patch antenna for increased bandwidth," *International Journal of Microwave and Wireless Technologies*, Vol. 5, No. 4, 529–535, 2013.

[45] Puri, I. and A. Agrawal, "Bandwidth and gain increment of microstrip patch antenna with shifted elliptical slot," *International Journal of Engineering Science and Technology*, Vol. 3, No. 7, 5539–5545, 2011.

[46] Maheshwari, S., P. Jain, and A. Agarwal, "CPW-fed wideband antenna with U-shaped ground plane," *International Journal of Wireless and Microwave Technologies*, Vol. 4, 25–31, 2014.

[47] Saraswat, R. and M. Kumar, "Implementation of the metamaterial multiband frequency reconfigurable antenna for IoT wireless standards," *IETE Journal of Research*, Vol. 70, No. 5, 4594–4605, 2023.

[48] Vaswani, J. and A. Agarwal, "A four port, dual band antenna for fifth generation mobile communication and WLAN services," *ACTA TECHNICA CORVINIENSIS — Bulletin of Engineering*, Vol. 13, No. 4, 73–76, 2020.

[49] Agarwal, A., M. Kumar, P. Jain, and S. Maheshwari, "Tapered circular microstrip antenna with modified ground plane for UWB communications," *International Journal of Electronics and Communication Engineering & Technology (IJECET)*, Vol. 4, No. 3, 43–47, 2013.

[50] Vaswani, J. and A. Agarwal, "Dual-band, dual-polarized two element slot antenna for fifth generation mobile devices," *Turkish Journal of Computer and Mathematics Education (TURCOMAT)*, Vol. 12, No. 3, 4822–4830, 2021.

[51] Vaswani, J. and A. Agarwal, "Twelve-port dual-polarized dual-band mimo antenna for fifth-generation mobile devices," *ICTACT Journal on Communication Technology*, Vol. 12, No. 3, 2490–2497, 2021.

[52] Saraswat, R. K. and M. Kumar, "A quad band metamaterial miniaturized antenna for wireless applications with gain enhancement," *Wireless Personal Communications*, Vol. 114, No. 4, 3595–3612, 2020.

[53] Bharti, G. and J. S. Sivia, "A design of multiband nested square shaped ring fractal antenna with circular ring elements for wireless applications," *Progress In Electromagnetics Research C*, Vol. 108, 115–125, 2021.

[54] Kaur, A. and P. K. Malik, "Multiband elliptical patch fractal and defected ground structures microstrip patch antenna for wireless applications," *Progress In Electromagnetics Research B*, Vol. 91, 157–173, 2021.

[55] Mu, W., Z. Wang, M. Yang, W. Nie, and P. Wang, "A six-port slot antenna system with wideband and high-isolation for 5G NR bands," *Progress In Electromagnetics Research M*, Vol. 107, 105–118, 2022.

[56] Jiang, J.-Y. and H.-L. Su, "A wideband eight-element MIMO antenna array in 5G NR n77/78/79 and WLAN-5 GHz bands for 5G smartphone applications," *International Journal of Antennas and Propagation*, Vol. 2022, No. 1, 8456936, 2022.

[57] Murugan, C. and T. Kavitha, "A compact four-element modified annular ring antenna for 5G applications," *Progress In Electromagnetics Research C*, Vol. 137, 169–183, 2023.

[58] Xue, J., G. Wang, S. Li, Z. Wang, and Q. Liang, "A metamaterial based dual-band UWB antenna design for 5G applications," *Progress In Electromagnetics Research M*, Vol. 127, 85–92, 2024.

[59] Neeshu, K. and A. K. Tiwary, "A compact, high gain ring metamaterial unit cell loaded triple band antenna for 5G application," *Progress In Electromagnetics Research M*, Vol. 124, 99–106, 2024.

[60] Mallani, H., A. Agrawal, and R. K. Saraswat, "Implementation of fractal metamaterial inspired antenna for multi-standard wireless applications," *Progress In Electromagnetics Research B*, Vol. 108, 121–137, 2024.

[61] Alpha Industries, ALPHA-6355 beamlead PIN diode, Data sheet (Online). Available: http://www.datasheetarchive.com/ALPHA-/PINdiode6355-datasheet.html.

[62] Abdollahvand, M., Y. Zehforoosh, B. Marufi, P. E. Kaleybar, and A. Dastranj, "A novel UWB in-body printed microstrip feed monopole antenna with dual band-stop capabilities," *Microwave and Optical Technology Letters*, Vol. 66, No. 9, e34317, 2024.

[63] Abdollahvand, M., B. A. Arand, K. Katoch, and S. Ghosh, "A novel and compact ultra-wideband printed monopole antenna

with enhanced bandwidth and dual-band stop properties," *Microwave and Optical Technology Letters*, Vol. 66, No. 1, e33990, 2023.

[64] Abdollahvand, M., H. R. Hassani, and G. R. Dadashzadeh, "Novel modified monopole antenna with band-notch characteristic for UWB application," *IEICE Electronics Express*, Vol. 7, No. 16, 1207–1213, 2010.

[65] Abdollahvand, M., K. Forooraghi, J. A. Encinar, Z. Atlasbaf, and E. Martinez-de Rioja, "Design and demonstration of a tri-band frequency selective surface for space applications in X, K, and Ka bands," *Microwave and Optical Technology Letters*, Vol. 62, No. 4, 1742–1751, 2020.

[66] Abdollahvand, M., G. R. Dadashzadeh, H. Ebrahimian, and M. Ojaroudi, "Compact ultra-wideband printed monopole antenna having frequency band-notch characteristic using defected ground structure," *Microwave and Optical Technology Letters*, Vol. 53, No. 10, 2363–2368, 2011.